Wideband Microstrip Antenna With Partially Open Cavity for 5G and Wi-Fi 6/6E Mobile Back-Cover Applications

Jinyue Zhang, Mingzhe Hu, *Graduate Student Member, IEEE*, Le Chang, *Senior Member, IEEE*, Yuehua Sun, Wenchao Wang, Zhijun Zhang, *Fellow, IEEE*, and Yue Li, *Senior Member, IEEE*

***Abstract*—A wideband microstrip antenna loaded with a partially open cavity is proposed for 5G and Wi-Fi 6/6E back-cover applications in mobile terminals. A partially open cavity, introduced at the patch center with a top slot, enables flexible excitation and coupling of multiple resonant modes. By integrating and manipulating the monopole, TM_{10}, TM_{01}, TM_{11}, and hybrid cavity modes, wideband radiation is realized without enlarging the footprint. The antenna attains an impedance bandwidth of 66.2% within a compact size of $21.5 \times 28 \times 2$ mm^3 ($0.27 \times 0.35 \times 0.025\ \lambda_L^3$, where λ_L is the free-space wavelength at the lowest frequency), yielding a high bandwidth-to-volume ratio (BVR) of 28.02. A four-element multiple-input multiple-output (MIMO) prototype was fabricated to validate its capability for high-capacity wireless communication in mobile terminals. The measured −6 dB-relative bandwidth achieves 68.5% (3.73–7.56 GHz), covering the 5G N79 and Wi-Fi 6/6E bands with isolation of over 12 dB. Benefiting from its wide bandwidth and compact volume, the proposed antenna offers a promising and feasible solution for back-cover integration in space-constrained mobile terminals.**

***Index Terms*—Cavity antennas, microstrip antennas, mobile antennas, multiple-input multiple-output (MIMO), wideband antennas.**

I. Introduction

The explosive growth of diverse wireless services has driven the demand for compact and wideband antennas in modern mobile terminals that can support multiple functions and communication standards within limited space [1], [2], [3], [4]. The metal bezel is commonly used for antenna design in conventional smartphones [5], [6], [7], [8], [9], [10], [11]. However, the ever-shrinking bezel and the denser antenna deployment have imposed severe space constraints, limiting both multiantenna implementation and wideband design. As a feasible alternative, the region beneath the mobile back-cover provides sufficient space for antenna deployment. With a low profile, a compact size, and ease of integration, microstrip antennas are well-suited for this scenario [12], [13], [14], [15], [16], [17], [18], [19]. However, traditional microstrip antennas suffer from narrow bandwidth due to their high quality factor and limited resonant modes, making them inadequate for the wideband requirements of modern wireless systems. Hence, extensive efforts have been devoted to overcoming the bandwidth limitation of microstrip antennas in recent years.

Existing bandwidth enhancement techniques can be broadly classified into three categories. The first category is based on parasitic elements such as stubs, patches, or stacked layers [20], [21], [22], [23], [24]. While these methods can broaden the impedance bandwidth, the resulting large size or high profile of the parasitic structures limits their applicability in mobile terminals. The second category employs metasurface-based structures composed of multiple patches or sectors, which inherently support multimodal operation [25], [26], [27]. In [27], [28], and [29], the patch was divided into four parts to excite the antiphase TM_{20} mode through slot coupling, and its coupling with the fundamental TM_{10} mode broadened the bandwidth. Moreover, characteristic mode analysis (CMA) has been employed to provide physical insight into metasurface structures, guiding the excitation of multiple modes for broadband design [30], [31]. However, these works generally suffer from a large size and feeding complexity, hindering their practical application in space-constrained mobile terminals. In [32], a tilted L-shaped probe was employed to excite a four-patch metasurface, leveraging the multimodal capability of the structure to achieve a 55.1% bandwidth with up to seven modes. Nevertheless, the bandwidth-to-volume ratio (BVR) was still limited to 7.22 owing to the relatively large footprint. The third category focuses on multimode manipulation, in which additional structures such as slots, notches, or vias are introduced to excite new modes and adjust their coupling, thereby achieving wideband operation [33], [34], [35], [36]. In [37], two sets of shorting vias and a pair of notches were employed to couple the monopole, $TM_{10,}$ and TM_{01} modes, yielding a bandwidth of 41.0%. In [38], four resonances based on electric and magnetic coupling were generated using vias and slots, leveraging the multimodal capability of the structure. In addition, the TM_{00} and TM_{10} modes were utilized to cover the 5G N79 band in [39], while the $TM_{0.5,0}$ and $TM_{0.5,1}$ modes

Received 12 November 2025; revised 28 February 2026; accepted 18 May 2026. Date of publication 2 June 2026; date of current version 6 August 2026. This work was supported in part by the National Key Research and Development Program of China under Grant 2021YFA0716601 and in part by the National Natural Science Foundation of China under Grant U22B2016. *(Corresponding author: Yue Li.)*

Jinyue Zhang, Mingzhe Hu, and Zhijun Zhang are with the Department of Electronic Engineering, Tsinghua University, Beijing 100084, China.

Le Chang is with Shaanxi Key Laboratory of Deep Space Exploration Intelligent Information Technology, School of Information and Communications Engineering, Xi'an Jiaotong University, Xi'an 710049, China.

Yuehua Sun and Wenchao Wang are with Transsion Company Ltd., Shanghai 200000, China.

Yue Li is with the Department of Electronic Engineering, Beijing National Research Center for Information Science and Technology, State Key Laboratory of Space Network and Communications, Tsinghua University, Beijing 100084, China (e-mail: lyee@tsinghua.edu.cn).

Digital Object Identifier 10.1109/TAP.2026.3696807

were pulled together to cover the Wi-Fi 6 band in [40]. Despite these efforts, achieving wideband coverage that includes both Wi-Fi and additional 5G bands for smartphone back-cover integration remains a challenge.

In this work, a wideband microstrip antenna loaded with a partially open cavity is proposed for terminal back-cover 5G and Wi-Fi 6/6E applications. A slotted rectangular cavity with partial side openings is implemented at the patch center. The cavity excites the monopole mode at a lower frequency, while at a higher frequency, an etched slot introduces a shared-aperture hybrid cavity mode, which can be tuned independently without disturbing the multiple microstrip modes. Meanwhile, the loaded cavity lowers the quality factors of the TM_{10} and TM_{01} modes and improves their impedance matching together with the TM_{11} mode. As a result, five resonances are combined to form a compact multimode response, achieving a −6 dB-relative bandwidth of 66.2% while maintaining a compact dimension of $21.5 \times 28 \times 2$ mm^3 ($0.27 \times 0.35 \times 0.025\ \lambda_L^3$, where λ_L is the free-space wavelength at the lowest frequency.), which yields a high BVR of 28.02 and fully covers the 5G N79 and Wi-Fi 6/6E bands. It should be noted that the −6 dB criterion is adopted here as it is widely acceptable for practical mobile terminal applications. Furthermore, a four-element multiple-input multiple-output (MIMO) prototype has been fabricated, and key performance metrics such as isolation, efficiency, and radiation pattern have been evaluated, demonstrating its suitability for high-capacity wireless communication in modern terminals.

The remainder of this article is organized as follows. Section II describes the structural configuration and operating principle of the proposed antenna. Section III presents the design evolution, the underlying mechanisms at each stage, and a parametric analysis. Section IV provides the measured results of the proposed MIMO antenna and makes a comparison with previously reported works, highlighting the advantages of the proposed design. Finally, Section V concludes this article.

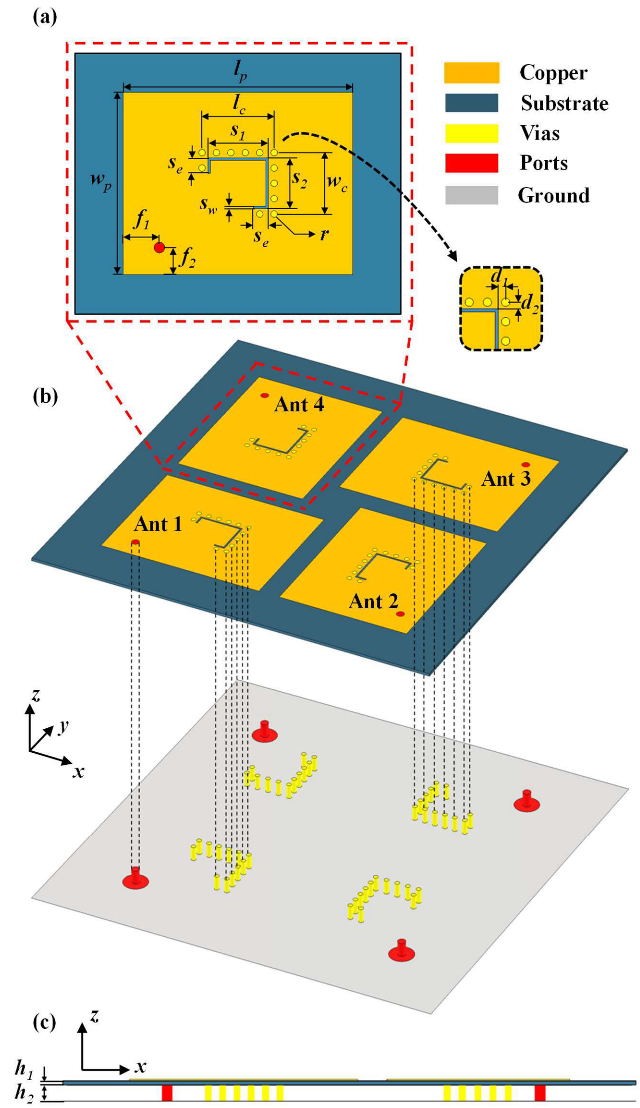

Fig. 1. Overall configuration of the proposed wideband antenna. (a) Top view of the antenna element. (b) Exploded view. (c) Cross-sectional view of the proposed four-element MIMO antenna.

II. Antenna Configuration

A. Overall Structure of the Antenna

Fig. 1 illustrates the configuration of the proposed antenna, which consists of two substrate layers: an FR-4 dielectric layer ($\varepsilon_r = 4.4$, $\tan\delta = 0.02$) with a thickness of $h_1 = 0.5$ mm, and an air-filled layer with a thickness of $h_2 = 1.5$ mm. Four antenna elements are placed in a sequential rotation arrangement to form the MIMO antenna. The enlarged view in the dashed box highlights a single antenna element, which is directly excited by a coaxial probe. Each element is based on a complete rectangular patch. At its center, a rectangular cavity is formed with metal posts, with one corner partially open toward the feeding side. In addition, a narrow slot is etched along the inner side of the cavity wall on the top surface. The entire structure employs only one metal layer on the top of the substrate.

B. Operation Principle of the Antenna Element

To illustrate the operating mechanism, an analysis is conducted on a single antenna element, whose characteristics are consistent with those in the final MIMO configuration. Fig. 1(a) shows its top view, with the optimized geometrical parameters summarized in Table I. The simulated reflection coefficient in Fig. 2 illustrates five resonances across a wide band of 3.78–7.52 GHz, labeled as Mode I–Mode V. The corresponding electric-field distributions at each resonant frequency shown in Fig. 2 provide physical insight into the identification and understanding of each resonant mode. At 4.18 GHz, Mode I exhibits a quasi-centrally symmetric electric-field distribution around the cavity, with the fields

TABLE I
Dimensions of the Antenna Element (Unit: mm)

Parameter	l_p	w_p	l_c	w_c	s_1	s_2	d_2
Value	28	21.5	8	7.9	7	6.8	0.15
Parameter	s_e	s_w	r	f_1	f_2	d_1	
Value	1.8	0.34	0.8	4.8	3.28	0.1	

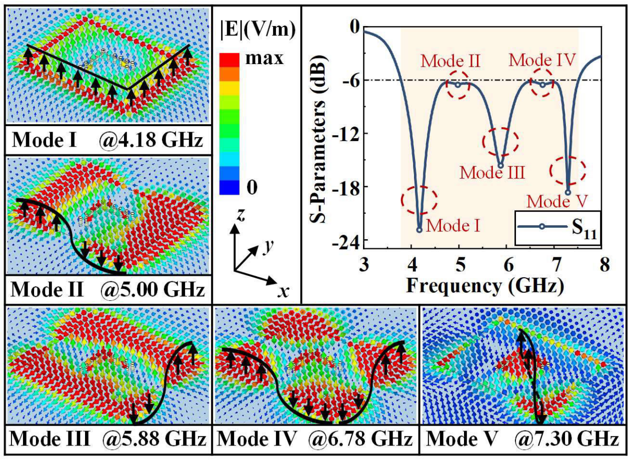

Fig. 2. Simulated reflection coefficient and the electric-field distributions of the proposed antenna element at the five resonant frequencies.

being in phase across the entire aperture. The uniform in-phase field along the patch edges forms a circular magnetic current source, generating a monopole mode. The electric-field distribution of Mode II at 5.00 GHz exhibits a half-wavelength electric-field distribution along the *x*-axis, with the fields on the two opposite edges out of phase, while remaining uniform along the *y*-axis. This behavior corresponds to the microstrip TM_{10} mode. Similarly, Mode III at 5.88 GHz can be regarded as an approximate 90° rotation of Mode II, showing a half-wavelength distribution along the *y*-axis while remaining uniform along the *x*-axis. This corresponds to the TM_{01} mode. At 6.78 GHz, Mode IV exhibits a half-wavelength variation along both the *x*- and *y*-axes, producing four distinct field lobes. The electric fields in diagonal quadrants are in phase, whereas those in adjacent quadrants are out of phase. This distribution corresponds to the TM_{11} mode. At 7.30 GHz, Mode V exhibits a hybrid resonance formed jointly by the partially open cavity and the patch, named the hybrid cavity mode. The electric field undergoes one reversal along an oblique path extending from the slot inside the cavity wall to the feed-side corner of the patch, which can be interpreted as the superposition of two orthogonal half-wavelength components along the *x*- and *y*-directions. As the central cavity participates in the resonance, the effective current path becomes shorter than that of the patch-only modes, leading to a higher resonant frequency. Together, the five resonant modes generated by the partially open cavity-loaded patch provide a compact multimode response that achieves a wide impedance bandwidth, fully covering the 5G N79 and Wi-Fi 6/6E bands for wireless communication.

III. Design Evolution and Mechanism Analysis

This section introduces the structural evolution leading to the generation and tuning of five resonant modes for wideband performance, along with the underlying mechanism associated with each design stage.

Fig. 3 illustrates the design process of the proposed antenna from Ant I to Ant III. Ant I represents the basic rectangular patch directly fed by a coaxial probe, serving as the initial reference. Within the frequency range of interest, Ant I demonstrates three resonances with poor impedance matching and a narrow bandwidth, with the lower two resonances (TM_{10} and TM_{01}) separated far from the TM_{11} mode, making wideband operation unattainable.

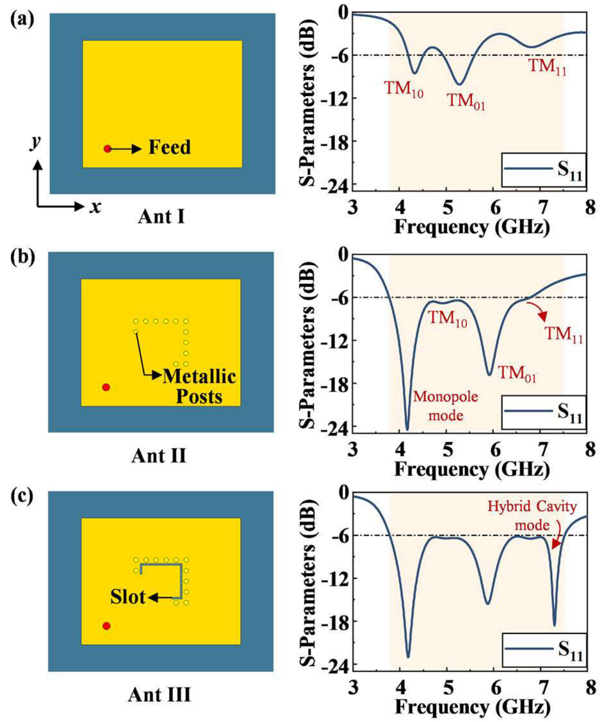

Fig. 3. Structural evolution of the proposed antenna and the corresponding reflection coefficients. (a) Ant I: conventional rectangular patch. (b) Ant II: partially open SIW cavity introduced at the patch center. (c) Ant III: A slot is etched on the patch, along the inner boundary of the cavity wall.

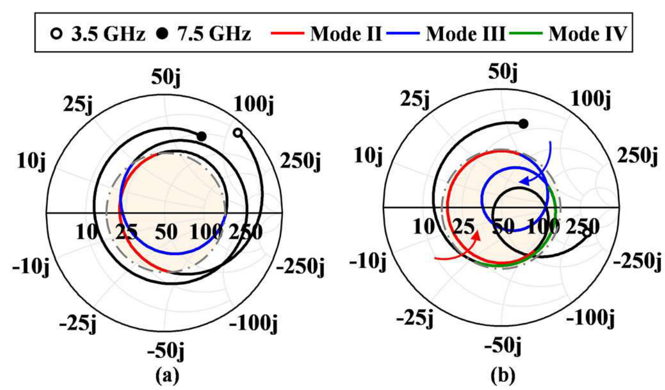

Fig. 4. Smith charts (3.5–7.5 GHz) of (a) Ant I and (b) Ant II.

Then, as shown in Fig. 3(b), Ant II incorporates a partially open cavity structure realized with metal posts for practical fabrication, which serves three major roles.

1) The partial opening allows the feeding energy to enter the cavity and excite vertical currents along its walls, which give rise to monopole-like radiation and introduce a new resonance below the fundamental TM_{10} mode.
2) The partially open cavity functions as a mode-dependent impedance loading structure introduced to the patch resonators. For the TM_{10} and TM_{01} modes, the cavity

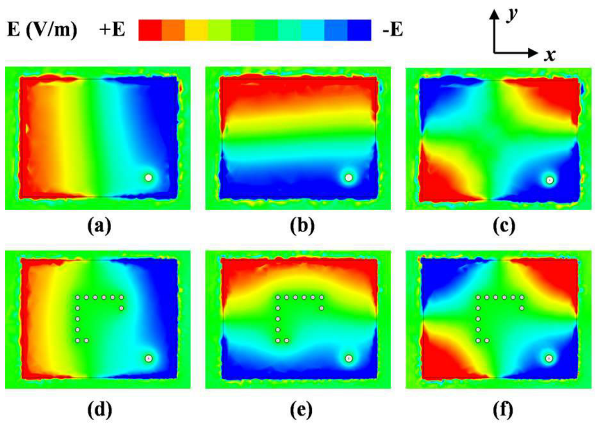

Fig. 5. Distinct tuning effects of the partially open cavity on different resonant modes. Electric-field of Ant I at (a) TM_{10} mode, (b) TM_{01} mode, (c) TM_{11} mode, and Ant II at (d) TM_{10} mode, (e) TM_{01} mode, and (f) TM_{11} mode.

introduces an effective parallel *LC* branch. The inductive contribution reduces the overall equivalent parallel inductance, shifting the resonant frequencies of the TM_{10} and TM_{01} modes upward. With the physical aperture unchanged, these frequency shifts effectively enlarge their electrical aperture, thereby lowering their quality factors and broadening the bandwidth. In addition, the introduced capacitive contribution provides an extra degree of freedom for impedance tuning. Both loading parameters can be tailored by adjusting the cavity dimensions, offering flexibility in optimizing bandwidth and matching. The Smith-chart variation in Fig. 4 illustrates these effects. In the regions corresponding to Modes II and III, the trajectory becomes tighter in Ant II, confirming the reduction in Q-factors and the expansion of impedance bandwidth. Moreover, the overall trajectory shifts closer to the chart center, which improves the matching of Mode IV (TM_{11}), with part of its locus moving inside the –6-dB circle compared with Ant I.

3) Besides the overall upward frequency shift, the partially open cavity provides an independent tuning capability for the patch-mode resonances. By adjusting the cavity dimensions (e.g., l_c and w_c), the TM_{10} and TM_{01} resonances can be tuned separately, while the TM_{11} resonance remains nearly unchanged. To clarify this behavior, the dominant z-directed electric field of the rectangular patch (Ant I) can be expressed in a general form as

$$E_{zmn}(x, y) = A_{mn} \sin\left(\frac{m\pi x}{l_p}\right) \sin\left(\frac{n\pi y}{w_p}\right) \quad (1)$$

where A_{mn} denotes the amplitude coefficient of the TM_{mn} mode. The field patterns corresponding to the TM_{10}, TM_{01}, and TM_{11} modes are illustrated in Fig. 5(a)–(c), showing half-wavelength variations along the *x*-, *y*-, and both directions, respectively. After introducing the central cavity, as shown in Fig. 5(d)–(f), the three modes exhibit distinct perturbations. Increasing l_c moves the cavity boundary toward the high-field regions of the TM_{10} mode, resulting in stronger loading and an upward resonance shift, while this mode remains insensitive to w_c because an electric-field null region exists along the central *y*-axis. On the contrary, varying w_c mainly affects TM_{01}, with little influence from l_c. For the TM_{11} mode, the field is concentrated near the four patch corners and remains minimal at the center region, so the central cavity has a negligible impact on its resonance. Consequently, placing the cavity at the weak-field center region enables independent tuning of TM_{10} and TM_{01} modes while preserving TM_{11} mode, facilitating modal alignment and wideband operation.

Finally, a narrow slot is etched along the inner side of the cavity wall on the patch top surface, generating Ant III, i.e., the proposed antenna, as shown in Fig. 3(c). This modification introduces a new high-frequency resonance that supplements the overall bandwidth while keeping the lower-frequency patch modes essentially unchanged. Its hybrid field distribution, jointly supported by the cavity wall and the patch, was previously illustrated in Fig. 2 (Mode V). The effect of the slot on the field distribution is explained in Fig. 6. Fig. 6(b) shows that without the slot, the cavity wall and patch rim provide short- and open-circuit terminations, supporting a 3/4-wavelength variation along the observation plane defined in Fig. 6(a). On the contrary, when the slot is introduced as shown in Fig. 6(c), the boundary at the cavity wall is forced to switch from a short to an open condition. Together with the patch rim, this forms a half-wavelength resonance, effectively lowering the resonant frequency for the same geometry. This enables the hybrid mode to couple with the preceding patch modes, thereby broadening the bandwidth. Meanwhile, the slot also serves as a radiation aperture, improving impedance matching. The resonant frequency of the hybrid cavity mode can be calculated as

$$f_{hyb} = \frac{c}{2a_{eff}\sqrt{\varepsilon_{eff}}}. \quad (2)$$

With the effective permittivity approximated by

$$\varepsilon_{eff} \approx \left(\frac{h_1}{h_1 + h_2}\right)\varepsilon_r + \left(1 - \frac{h_1}{h_1 + h_2}\right) \cdot 1 \quad (3)$$

while a_{eff} represents the effective electrical length of the hybrid resonance, which is estimated as 15.49 mm by geometrically combining the effective dimensions along the *x*- and *y*-directions. The calculated f_{hyb} = 7.12 GHz agrees well with the full-wave simulations in Fig. 3(c). Small deviations arise from the edge effect of the metal posts and the partial opening.

The Smith charts in Fig. 7 confirm that the slot introduces an additional loop near 7.3 GHz corresponding to Mode V, while the rest of the trajectory remains almost unchanged. This indicates that the newly added hybrid resonance supplements the high-frequency side without disturbing the lower patch modes. At low frequencies, the fields inside the cavity are weak near the slot region and are further shielded by the cavity walls, so the slot perturbation has little impact. On the contrary, at higher frequencies, the cavity fields become evident, and the slot locally modifies the boundary condition, enabling the excitation of Mode V. Consequently, the hybrid mode can

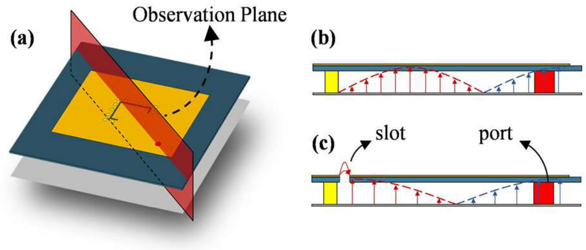

Fig. 6. (a) Perspective view of Ant III and the observation plane. Cross-section of the electric-field distribution within the observation plane (b) without a slot and (c) with a slot.

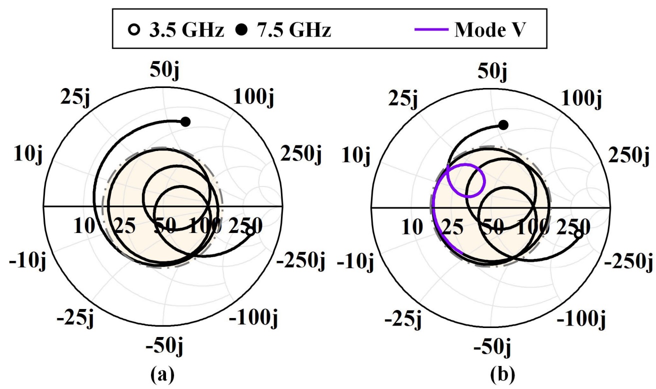

Fig. 7. Smith charts (3.5–7.5 GHz) of (a) Ant II and (b) Ant III.

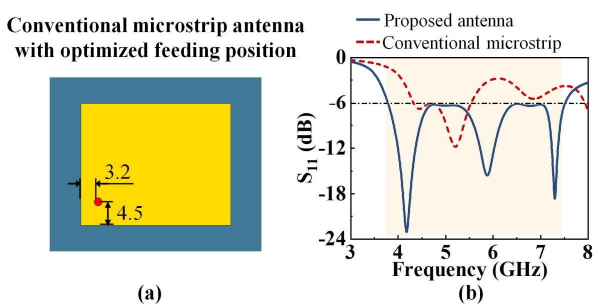

Fig. 8. Comparison of the proposed antenna element and a conventional microstrip antenna with the same dimensions. (a) Conventional microstrip antenna (unit: mm). (b) S_{11} comparison.

be independently tuned without affecting the lower modes, effectively realizing a shared-aperture wideband design.

By rationally exciting and independently tuning the five resonant modes, the proposed antenna achieves a compact multimode response with significantly enhanced bandwidth. Fig. 8 further compares the proposed antenna element with a conventional microstrip antenna of the same dimensions, where the feed position is optimized for the best matching (with a fractional bandwidth of 24.6%). While the conventional patch only supports narrow resonances, the proposed antenna significantly broadens the bandwidth, achieving approximately 270% of that of the conventional microstrip antenna with the same aperture, representing a substantial improvement. In addition, owing to the zeroth-order-like field distribution induced by the monopole mode, the lowest operating frequency is shifted downward by 12.5% while

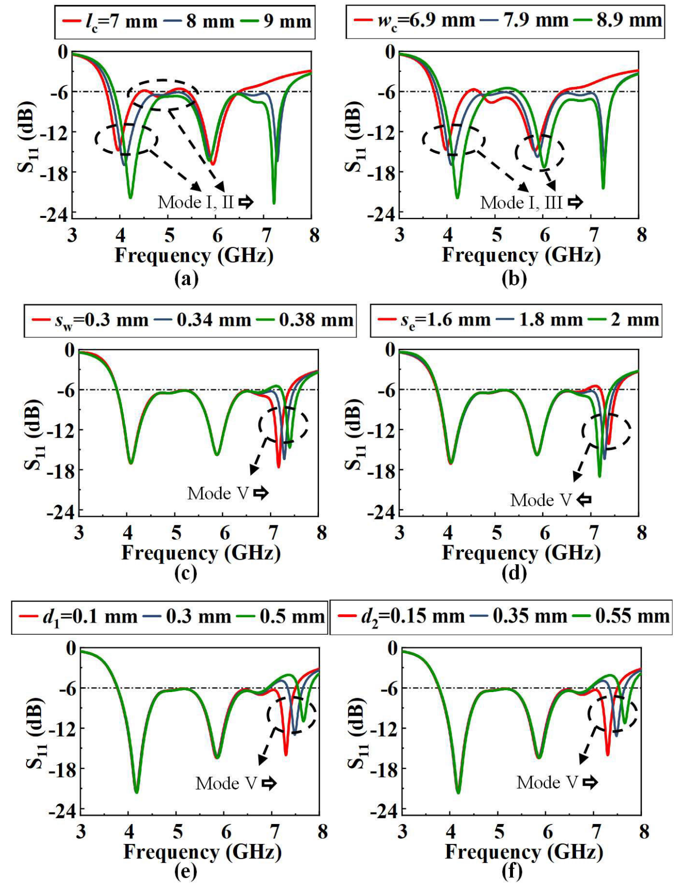

Fig. 9. Reflection coefficient for different parameters of the proposed antenna element. (a) l_c. (b) w_c. (c) s_w. (d) s_e. (e) d_1. (f) d_2.

maintaining patch integrity, contributing to structural miniaturization.

To demonstrate the controllability of these resonances, several critical parameters are analyzed. Fig. 9(a) illustrates the reflection coefficient when varying the cavity length, l_c. As l_c increases, the perturbation of the electric field shifts the TM_{10} mode (Mode II) upward, while the TM_{01} mode (Mode III) remains nearly unchanged, consistent with the previous analysis. Meanwhile, the monopole mode (Mode I) also shifts upward due to the reduced parallel inductance. Similarly, as shown in Fig. 9(b), varying the cavity width, w_c mainly tunes the monopole and TM_{01} modes, while leaving TM_{10} nearly unchanged. As a result, the frequency spacing among Mode I, Mode II, Mode III, and the TM_{11} mode (Mode IV) can be effectively adjusted, providing additional flexibility in tailoring their coupling and achieving the wideband response. Fig. 9(c) and (d) present the influence of slot parameters on the hybrid cavity mode (Mode V). Increasing the slot width, s_w reduces the a_{eff} in (2), thereby raising the resonant frequency of Mode V. On the other hand, varying the slot extension s_e mainly alters the coupling between the feed and the cavity, which also shifts the resonant frequency. Furthermore, Fig. 9(e) and (f) evaluate the influence of the slot distances from adjacent cavity walls (d_1 and d_2) on Mode V. Similarly, increasing d_1 and d_2 shortens the effective electrical length a_{eff}, driving the resonance of Mode V to higher fre-

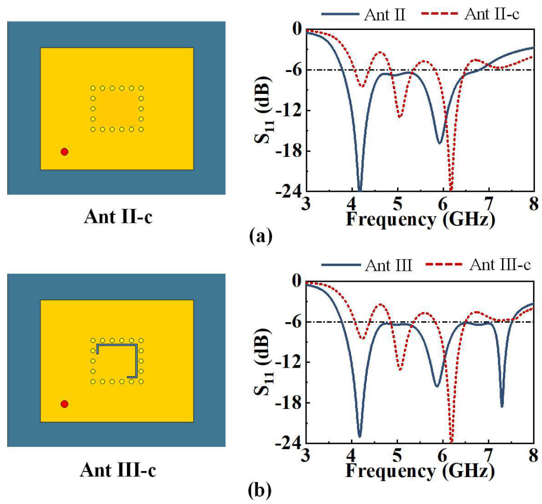

Fig. 10. Simulated reflection coefficients of the proposed partially open cavity antennas versus the closed-cavity reference antennas. (a) Configuration of the completely closed Ant II-c and its S-parameter comparison with Ant II. (b) Configuration of the completely closed Ant III-c and its S-parameter comparison with Ant III.

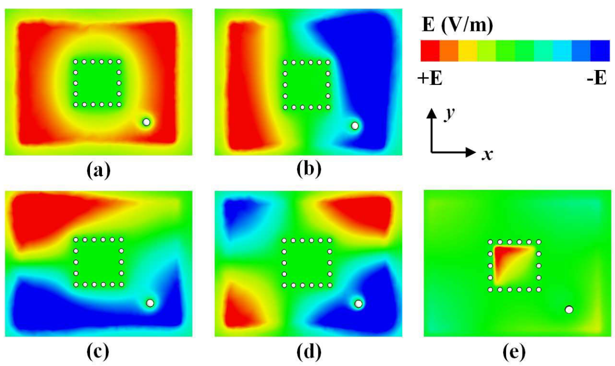

Fig. 11. Simulated electric-field distributions of the completely closed-cavity reference antennas. Ant II-c at (a) 4.22 GHz, (b) 5.05 GHz, (c) 6.17 GHz, (d) 7.22 GHz, and (e) Ant III-c at 7.57 GHz.

quencies. In all these cases, the lower modes remain essentially unchanged, confirming that Mode V can be independently tuned without disturbing the other resonances.

While the above analysis comprehensively elucidates the mechanisms of wideband multimode excitation and the flexible tunability of the individual modes, this entire wideband operation is fundamentally predicated on the partially open architecture of the cavity. To further elucidate this underlying mechanism and validate the absolute necessity of the partially open configuration, a completely closed cavity is simulated for comparison. As shown in the S-parameters and electric-field distributions in Figs. 10 and 11, respectively, completely enclosing the cavity severely disrupts the wideband multimode operation.

First, regarding the monopole mode, fully enclosing the cavity eliminates the essential coupling aperture near the feed, causing strong reactive reflections that deteriorate its impedance matching and excitation efficiency. Second, for the microstrip modes, the enclosed walls near the feed induce significant backscattering, resulting in an unbalanced energy

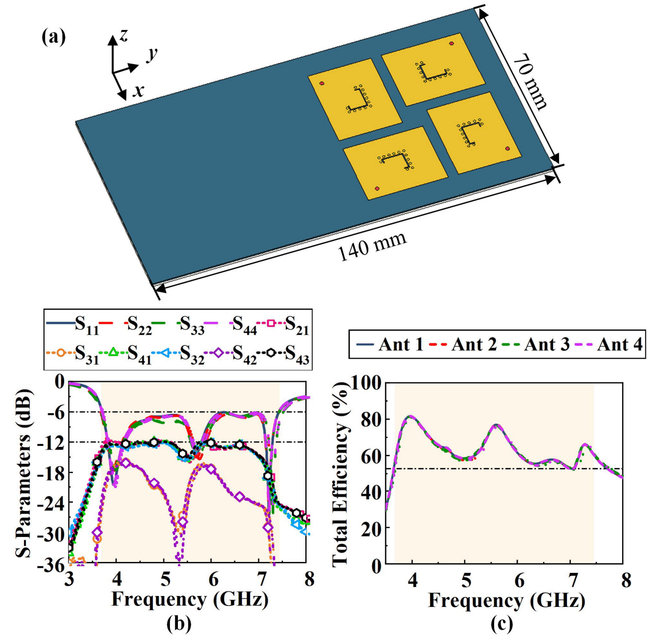

Fig. 12. Analysis of the proposed four-element MIMO antenna integrated on a common ground layer. (a) Configuration. (b) Reflection and transmission coefficient. (c) Total efficiencies.

distribution with stronger fields on the feeding side, as demonstrated in Fig. 11(b)–(d). This unbalanced distribution reduces the effective resonant size of the patch, shifting the resonant frequencies of the TM modes upward and away from their targeted bands. Simultaneously, the suppressed fields in the central region significantly increase the modal Q-factors, leading to much sharper resonances that deteriorate the continuous wideband matching. Finally, for the closed Ant III-c, the solid metal walls block the primary energy injection path, causing the original hybrid cavity mode (Mode V) to vanish. As observed in Fig. 10(b), a newly emerged, extremely weak parasitic resonance appears near 7.57 GHz. This occurs because the excitation energy couples into the top slot through weak spatial radiation, exciting a quasi-diagonal quarter-wavelength resonance in the cavity, dictated by the open-circuit boundary at the slot and the short-circuit boundary at the newly closed walls. The resonant frequency can be calculated as

$$f_{cav} = \frac{c}{4a_{cav}\sqrt{\varepsilon_{eff}}} \tag{4}$$

where a_{cav} represents the effective electrical length of the slotted cavity (estimated from the slot to the cavity edge). The calculated f_{cav} = 7.77 GHz agrees well with the simulation results, which is further validated by the field distribution in Fig. 11(e). Due to its inherently weak coupling and excessively high frequency, this parasitic mode fails to merge with the fundamental modes to form a wideband performance.

In summary, this comparative study conclusively demonstrates that the partially open architecture is governed by clear physical mechanisms rather than trial-and-error, proving essential for maintaining the required modal field balance and ensuring continuous wideband impedance matching.

Based on the proposed antenna element, a 4 × 4 MIMO configuration is implemented to verify its suitability for

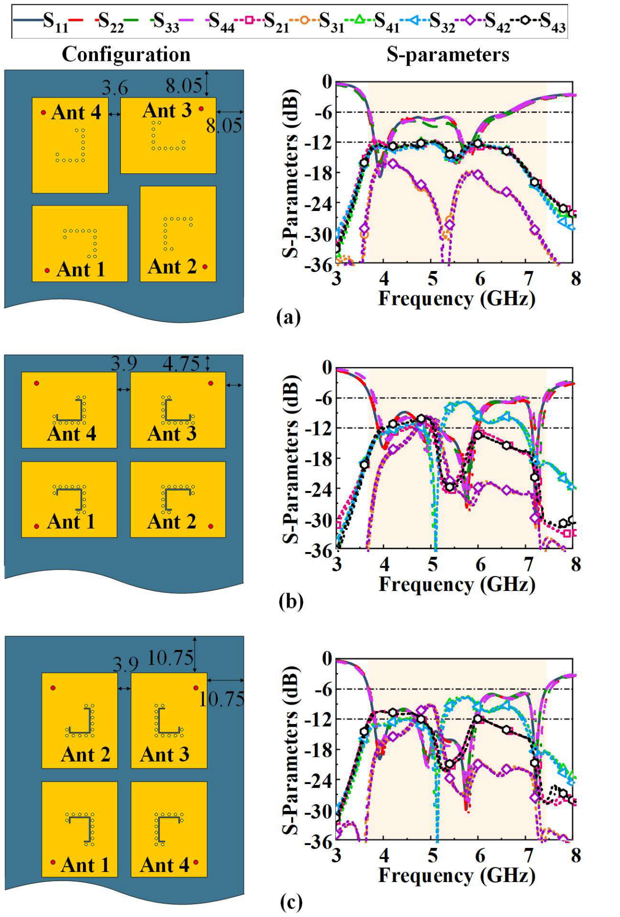

Fig. 13. Simulated S-parameters of the MIMO arrays on a mobile ground under different configurations for comparative analysis. (a) Ant II with the proposed rotationally symmetric layout. (b) Ant III with a centrosymmetric horizontal layout. (c) Ant III with a centrosymmetric vertical layout (unit: mm).

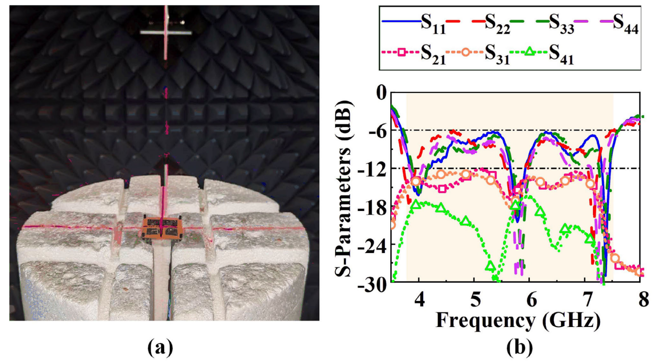

Fig. 14. (a) Prototype and measurement environment. (b) Measured reflection and transmission coefficients of the proposed MIMO antenna.

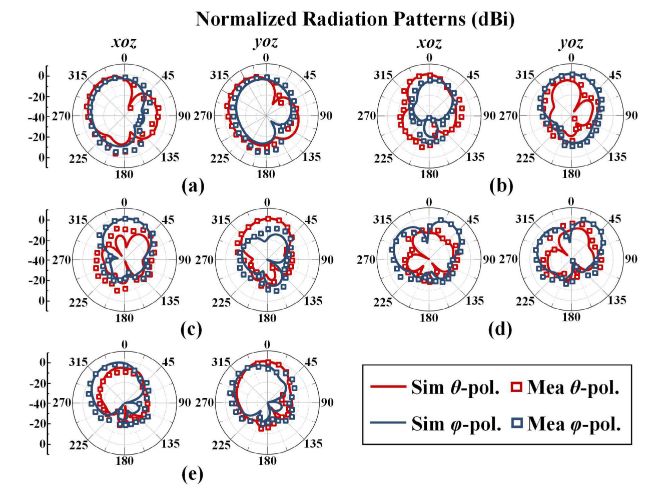

Fig. 15. Simulated and measured 2-D radiation patterns of the proposed four-element MIMO antenna at (a) 4.18, (b) 5.0, (c) 5.88, (d) 6.78, and (e) 7.3 GHz.

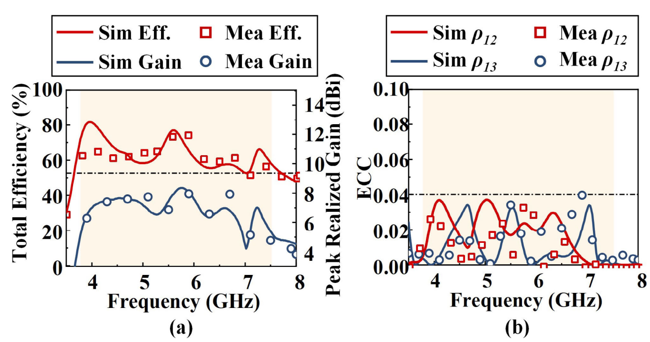

Fig. 16. (a) Total efficiencies and peak realized gains of the proposed MIMO antenna in simulated and measured results. (b) Simulated and measured ECCs of the proposed four-element MIMO antenna.

high-capacity wireless communications in modern terminals, as shown in Fig. 1(b) and (c), with an element spacing d_m = 3.6 mm and a substrate dimension l_{sub} = 70 mm. To accommodate the impedance and coupling conditions in the MIMO environment, the central cavity dimensions are slightly adjusted to l_c = 8.8 mm, w_c = 5.5 mm, s_1 = 7.4 mm, s_2 = 6.2 mm, and s_e = 1.85 mm, without altering the fundamental design concept. For practical validation, the MIMO antenna is simulated on a ground plane of 140×70 mm^2, representing the typical size of a smartphone as illustrated in Fig. 12(a). Fig. 12(b) and (c) present the simulated S-parameters and total efficiencies of the proposed MIMO antenna. All four elements exhibit a −6-dB impedance bandwidth from 3.71 to 7.44 GHz, with interelement isolation better than 12 dB. The total efficiency exceeds 53% over the entire band, confirming low loss and good radiation performance in a mobile back-cover environment.

To explicitly clarify the underlying decoupling mechanism of the achieved high isolation, a comparative study of different array configurations is conducted, as shown in Fig. 13. Note that all evaluated arrays occupy the same overall footprint and maintain identical distances to the ground edges for a fair comparison. As illustrated in Fig. 13(a), when utilizing Ant II as the unit element in the proposed rotationally symmetric layout, except for the disappearance of Mode V, the array still maintains high isolation across the operating bands. This implies that the spatial layout itself provides the dominant decoupling contribution. Conversely, when the proposed Ant III elements are arranged in conventional centrosymmetric layouts, either horizontally [see Fig. 13(b)] or vertically [see Fig. 13(c)] aligned, the mutual coupling deteriorates significantly. This severe coupling stems from the direct

TABLE II
COMPARISONS OF THE PROPOSED ANTENNA WITH OTHER MINIATURIZED MICROSTRIP ANTENNAS

Ref.	-6 dB Bandwidth	Element Dimension (λ_L^3)	BVR (λ_L^{-3})	Isolation (dB)	Total efficiency
[25]	~5.00-7.20 GHz (36.1%)*	0.87 × 0.87 × 0.050	0.95	—	78%-97%
[26]	~3.02-5.72 GHz (66.1%)*	0.87 × 0.87 × 0.120	0.73	—	N. P.
[15]	4.40-5.04 GHz (13.6%)	0.59 × 0.30 × 0.012	6.40	> 18	42%-86%
[38]	3.14-4.33 GHz (31.9%)	0.68 × 0.29 × 0.015	10.63	—	>61.7%
	3.20-4.33 GHz (30.3%)	0.53 × 0.36 × 0.011	13.64		>60.3%
[40]	5.13-5.86 GHz (13.3%)	0.25 × 0.12 × 0.034	13.04	> 10.8	45%-65%
[35]	3.30-4.20 GHz (24.0%)	0.44 × 0.44 × 0.026	4.77	> 10	42%-61%
[37]	3.30-5.00 GHz (41.0%)	0.32 × 0.28 × 0.028	16.33	> 12	55%-82%
[32]	5.14-9.05 GHz (55.1%)	0.51 × 0.44 × 0.034	7.22	> 12	44%-85%
[41]	~3.45-3.80 GHz (9.7%)/ 4.52-4.90 GHz (8.1%)*	0.29 × 0.25 × 0.051	/	> 14	60%-86%
[42]	~2.20-2.70 GHz (20.4%)/ 5.00-6.25 GHz (22.2%)*	0.44 × 0.37 × 0.049	/	> 15.3	48%-82%
Pro.	**3.78-7.52 GHz (66.2%)**	**0.35 × 0.27 × 0.025**	**28.02**	**> 12**	**53%-82%**

*: The -6 dB bandwidths are visually estimated from the S-parameter curves provided in the original papers.
—: Only single antenna has been proposed.
/: Not applicable (N/A) for dual-band antennas.
N. P.: Not provided.

alignment of their radiation apertures in specific modes. For instance, at the TM_{10} resonant frequency, Ants 1 & 2 (and 3 & 4) are arranged along the E-plane with their radiation apertures adjacent to each other, leading to strong coupling, so that the S_{21} and S_{43} are worse than −10 dB. Similarly, at the TM_{01} resonance, the S_{41} and S_{32} degrade to nearly −7 dB. Therefore, the proposed rotationally symmetric layout enforces spatial orthogonality, preventing the primary radiation apertures from facing each other directly. This effectively eliminates the strong copolarized coupling paths and suppresses mutual interference.

IV. FABRICATION AND MEASUREMENT

A prototype of the proposed four-element MIMO antenna was fabricated and tested to validate the design. The metal layer was fabricated on an FR-4 substrate through the printed circuit board (PCB) process, and the board was elevated by four nylon pillars at its corners to form the air layer and provide mechanical support. Metallized vias were drilled on the patch to emulate the cavity walls, as well as to accommodate the feeding probe. To simplify fabrication while maintaining performance, an FR-4 board with copper cladding on both sides was employed as the ground plane. Four metallized holes were implemented on the ground plane through which the subminiature A (SMA) inner conductors passed and extended to contact the top patch for excitation, while the outer conductors were soldered to the ground. A photograph of the fabricated prototype and the measurement setup is shown in Fig. 14(a), where testing was conducted using an N9917A vector network analyzer and a standard microwave anechoic chamber.

Fig. 14(b) illustrates the measured S-parameters of the fabricated prototype. The measured reflection coefficients of all four ports exhibit a –6-dB bandwidth from 3.73 to 7.56 GHz (68.5%) with isolation better than 12 dB, in good agreement with the simulated results.

The measured radiation patterns at the five resonant frequencies are presented in Fig. 15. Due to the structural symmetry, only the results of Ant 1 are presented as representative. The coordinate orientation follows the definition provided in Fig. 1. The measured patterns for both θ- and φ-polarizations in the *xoz* and *yoz* planes exhibit good agreement with the simulated results, validating the accuracy of the proposed design. For cases shown in Fig. 15(a) and (d), the monopole and TM_{11} modes exhibit a near-conical radiation pattern, while in (b), (c), and (e), the TM_{10}, TM_{01}, and the hybrid cavity modes show broadside radiation behavior, consistent with the theoretical analysis, and acceptable for mobile terminals. The slight beam tilt observed in the element patterns is attributed to the array configuration, which is actually advantageous for achieving wide-angle coverage in MIMO wireless communication terminals.

Fig. 16(a) presents the total efficiency and the peak realized gain. Due to the structural symmetry, only the results of Ant 1 are shown as representative. The measured results agree well with the simulated ones. Within the frequency band of interest, the antenna achieves a realized gain of 4.2–8.3 dBi, satisfactory for mobile terminal antenna applications.

Fig. 16(b) illustrates the envelope correlation coefficients (ECCs) extracted from the radiation patterns. The measured results show good agreement with their simulated counterparts, and both ρ_{12} and ρ_{13} are smaller than 0.05, which is sufficiently low for MIMO antenna applications in mobile terminals.

To further validate the superiority of the proposed design, Table II provides a comparative summary of key performance metrics between the proposed antenna and several recently reported miniaturized microstrip antennas. It should be noted that only a limited number of existing works simultaneously achieve broadband operation and a compact geometry suitable for terminal back-cover integration. The antennas reported in [25] and [26] exhibit wide impedance bandwidths. However, their metasurface-based structures occupy a large physical aperture, making them unsuitable for smartphone integration and difficult to configure in MIMO systems. Furthermore, their BVRs are relatively low due to the bulky design. The antennas presented in [15], [38], and [40] feature low-profile or compact footprints that are easy to integrate into terminal platforms, but their operating bandwidths are rather limited, which consequently constrains their BVR performance. In addition, recent dual-band MIMO designs [41], [42], and [43] have been proposed for specific Wi-Fi and 5G bands. However, they generally suffer from relatively high profiles and discontinuous operating bandwidths, failing to provide continuous wideband coverage. Furthermore, the design in [43] relies on a 3-D structural configuration, which significantly increases the integration difficulty in space-constrained mobile terminals. Compared with the wideband MIMO microstrip antennas reported in [32], [35], and [37], the proposed design achieves significant improvements in both bandwidth and size reduction, resulting in a high BVR of 28.02 while maintaining desirable isolation and radiation efficiency.

In conclusion, the proposed antenna effectively balances wideband performance and compact size, covering the entire 5G N79 and Wi-Fi 6/6E bands while maintaining a single-metal-layer configuration that facilitates manufacture, demonstrating strong competitiveness among existing miniaturized MIMO antenna solutions.

V. Conclusion

A wideband and compact microstrip antenna with a partially open cavity is proposed for 5G N79 and Wi-Fi 6/6E terminal applications. The antenna employs a single-layer patch in which a partially open cavity is introduced at the center, and a top slot is etched to excite an additional hybrid mode. The incorporation of the partially open cavity enables efficient multimode coupling and bandwidth enhancement without increasing the overall antenna footprint, thereby maintaining a compact structure. By simultaneously exciting and tuning the monopole, TM_{10}, TM_{01}, TM_{11}, and hybrid cavity modes, wideband radiation is achieved within a compact element size of $21.5 \times 28 \times 2$ mm^3 ($0.27 \times 0.35 \times 0.025\ \lambda_L^3$). A four-element MIMO configuration is developed to verify the design's integration feasibility on the terminal back cover. The fabricated prototype exhibits an extremely wide measured −6 dB impedance bandwidth of 68.5% (3.73–7.56 GHz), fully covering the 5G N79 and Wi-Fi 6/6E bands with a high BVR of 28.99. The measured total efficiencies range from 53% to 82%, and the port isolations are better than 12 dB, with stable radiation characteristics and ECCs below 0.05 across the operating band. With its advantages of broad bandwidth, a compact geometry, a low profile, and ease of integration, the proposed design demonstrates strong competitiveness and practical potential for compact mobile terminals supporting diverse frequency bands and wireless services.

References

[1] M. Chen, L. Chang, and A. Zhang, "Wideband antenna pairs consisting of E-/M-coupling frame monopoles and M-/E-coupling back cover patches for mobile terminal applications," *IEEE Trans. Antennas Propag.*, vol. 72, no. 2, pp. 1308–1318, Feb. 2024.

[2] I. R. R. Barani, K.-L. Wong, Y.-X. Zhang, and W.-Y. Li, "Low-profile wideband conjoined open-slot antennas fed by grounded coplanar waveguides for 4 × 4 5G MIMO operation," *IEEE Trans. Antennas Propag.*, vol. 68, no. 4, pp. 2646–2657, Apr. 2020.

[3] Y. Wang and Z. Du, "Wideband monopole antenna with less nonground portion for octa-band WWAN/LTE mobile phones," *IEEE Trans. Antennas Propag.*, vol. 64, no. 1, pp. 383–388, Jan. 2016.

[4] S. Wang et al., "Antenna thousandfold miniaturization with ohmic-biased transistor circuit," *Electromagn. Sci.*, vol. 3, no. 2, Jun. 2025, Art. no. 0100583-12.

[5] Q. Chen et al., "Single ring slot-based antennas for metal-rimmed 4G/5G smartphones," *IEEE Trans. Antennas Propag.*, vol. 67, no. 3, pp. 1476–1487, Mar. 2019.

[6] L. Sun, Y. Li, Z. Zhang, and Z. Feng, "Wideband 5G MIMO antenna with integrated orthogonal-mode dual-antenna pairs for metal-rimmed smartphones," *IEEE Trans. Antennas Propag.*, vol. 68, no. 4, pp. 2494–2503, Apr. 2020.

[7] A. Zhang, K. Wei, and Z. Zhang, "Multiband and wideband self-multipath decoupled antenna pairs," *IEEE Trans. Antennas Propag.*, vol. 71, no. 7, pp. 5605–5615, Jul. 2023.

[8] Z. Xu and C. Deng, "High-isolated MIMO antenna design based on pattern diversity for 5G mobile terminals," *IEEE Antennas Wireless Propag. Lett.*, vol. 19, pp. 467–471, 2020.

[9] P. Li, Y. Zhang, X. Qin, P. Liang, K. Wei, and Y. Li, "Axial-ratio bandwidth enhancement of circular-polarized bezel antennas using a parasitic capacitive strip for mobile satellite communications," *IEEE Trans. Antennas Propag.*, vol. 73, no. 3, pp. 1846–1851, Mar. 2025.

[10] M. Stanley, Y. Huang, H. Wang, H. Zhou, Z. Tian, and Q. Xu, "A novel reconfigurable metal rim integrated open slot antenna for octa-band smartphone applications," *IEEE Trans. Antennas Propag.*, vol. 65, no. 7, pp. 3352–3363, Jul. 2017.

[11] W. Zhao and Y. Wang, "A shared-branch eleven-band mobile antenna with a 0.5-mm clearance for metal-bezel mobile phones covering all the 4G LTE and 5G NR bands," *IEEE Trans. Antennas Propag.*, vol. 72, no. 4, pp. 3748–3753, Apr. 2024.

[12] K.-L. Wong, J.-Z. Chen, and W.-Y. Li, "Four-port wideband annular-ring patch antenna generating four decoupled waves for 5G multi-input–multi-output access points," *IEEE Trans. Antennas Propag.*, vol. 69, no. 5, pp. 2946–2951, May 2021.

[13] S. Gao, L. Chang, A. Zhang, Y. Li, and Z. Zhang, "Small-volume microstrip patch antennas exactly covering Wi-Fi 6 bands of 2.4–2.5 GHz and 5.15–5.85 GHz," *IEEE Trans. Antennas Propag.*, vol. 71, no. 7, pp. 5739–5748, Jul. 2023.

[14] X. Zhai, L. Zhu, and Q. Liu, "A low-profile vertically polarized patch antenna with wideband omnidirectional radiation based on triple resonant modes," *IEEE Antennas Wireless Propag. Lett.*, vol. 24, pp. 73–77, 2025.

[15] B. Cheng and Z. Du, "A wideband low-profile microstrip MIMO antenna for 5G mobile phones," *IEEE Trans. Antennas Propag.*, vol. 70, no. 2, pp. 1476–1481, Feb. 2022.

[16] A. Zhang, K. Wei, Y. Hu, and Q. Guan, "High-isolated coupling-grounded patch antenna pair with shared radiator for the application of 5G mobile terminals," *IEEE Trans. Antennas Propag.*, vol. 70, no. 9, pp. 7896–7904, Sep. 2022.

[17] W. Hu et al., "Wideband back-cover antenna design using dual characteristic modes with high isolation for 5G MIMO smartphone," *IEEE Trans. Antennas Propag.*, vol. 70, no. 7, pp. 5254–5265, Jul. 2022.

[18] L. Chang and H. Wang, "Dual-band four-antenna module covering N78/N79 based on PIFA for 5G terminals," *IEEE Antennas Wireless Propag. Lett.*, vol. 21, pp. 168–172, 2022.

[19] Q.-L. Yan, N.-W. Liu, L. Zhu, Y. Yun, and Y. Liu, "Pattern transformation of low-profile multi-mode antenna for a phased array with simultaneous wide-angle scanning and high-gain properties," *IEEE Trans. Antennas Propag.*, vol. 73, no. 8, pp. 5514–5522, Aug. 2025.

[20] T.-Y. Yan, X.-H. Ding, J.-Y. Yang, and J.-X. Chen, "A low-cost compact dual-polarized patch antenna array for 5G massive MIMO base station," *IEEE Antennas Wireless Propag. Lett.*, vol. 23, pp. 1381–1385, 2024.

[21] H. Huang, X. Li, and Y. Liu, "A low-profile, dual-polarized patch antenna for 5G MIMO application," *IEEE Trans. Antennas Propag.*, vol. 67, no. 2, pp. 1275–1279, Feb. 2019.

[22] Z. Shao, L.-F. Qiu, and Y. P. Zhang, "Design of wideband differentially fed multilayer stacked patch antennas based on bat algorithm," *IEEE Antennas Wireless Propag. Lett.*, vol. 19, pp. 1172–1176, 2020.

[23] J. Hao, N. Yan, Y. Luo, H. Fu, and K. Ma, "A low-cost dual-band multimode high-gain stacked-patch antenna based on SISL for 5G applications," *IEEE Antennas Wireless Propag. Lett.*, vol. 21, pp. 4–8, 2022.

[24] X. Liu, M. Hu, Y. Zhang, P. Wu, H. Wang, and Y. Li, "Solving the efficiency-dip problem of adding parasitic elements for ultrathin microstrip antennas," *IEEE Trans. Antennas Propag.*, vol. 73, no. 8, pp. 5075–5082, Aug. 2025.

[25] J. d. Dieu Ntawangaheza et al., "A single-layer low-profile broadband metasurface-inspired antenna with monopole-like radiation characteristics," *IEEE Trans. Antennas Propag.*, vol. 70, no. 6, pp. 4818–4823, Jun. 2022.

[26] Y. Luo, Y. Wang, N. Yan, W. An, and K. Ma, "A broadband gain-enhanced conical-beam antenna loaded with the multicircle sectored metasurface," *IEEE Trans. Antennas Propag.*, vol. 71, no. 7, pp. 5542–5548, Jul. 2023.

[27] Y. Zhang and Y. Li, "Wideband microstrip antenna in small volume without using fundamental mode," *Electromagn. Sci.*, vol. 1, no. 2, pp. 1–6, Jun. 2023.

[28] W. Sun, Y. Li, Z. Zhang, and P.-Y. Chen, "Low-profile and wideband microstrip antenna using quasi-periodic aperture and slot-to-CPW transition," *IEEE Trans. Antennas Propag.*, vol. 67, no. 1, pp. 632–637, Jan. 2019.

[29] W. Sun, Y. Li, L. Chang, H. Li, X. Qin, and H. Wang, "Dual-band dual-polarized microstrip antenna array using double-layer gridded patches for 5G millimeter-wave applications," *IEEE Trans. Antennas Propag.*, vol. 69, no. 10, pp. 6489–6499, Oct. 2021.

[30] Z. Wang, F. Fan, R. Li, Y. Mo, J. Li, and X. Zhao, "A dual-band wideband U-slot resonant metasurface antenna array for millimeter-wave applications using characteristic mode analysis," *IEEE Trans. Antennas Propag.*, vol. 73, no. 8, pp. 5217–5222, Aug. 2025.

[31] S. Liu, D. Yang, L. Wu, K. Sun, J. Hu, and Y. Chen, "A dual-polarized omnidirectional metasurface antenna designed via characteristic mode analysis," *IEEE Antennas Wireless Propag. Lett.*, vol. 22, pp. 1010–1014, 2023.

[32] K. Li, Y. Zhang, and Y. Li, "Hepta-mode terminal microstrip antenna for mobile Wi-Fi 6/6E and UWB channels 5–11 MIMO applications," *IEEE Trans. Antennas Propag.*, vol. 72, no. 9, pp. 7048–7056, Sep. 2024.

[33] N.-W. Liu, L. Zhu, and W.-W. Choi, "A differential-fed microstrip patch antenna with bandwidth enhancement under operation of TM10 and TM30 modes," *IEEE Trans. Antennas Propag.*, vol. 65, no. 4, pp. 1607–1614, Apr. 2017.

[34] H. Zhang, L. Chang, and A. Zhang, "Low-profile and dual-band microstrip patch antenna based on magnetic coupling covering Wi-Fi 6 bands for mobile terminals," *IEEE Antennas Wireless Propag. Lett.*, vol. 24, pp. 1899–1903, 2025.

[35] K.-L. Wong, M.-F. Jian, and W.-Y. Li, "Low-profile wideband four-corner-fed square patch antenna for 5G MIMO mobile antenna application," *IEEE Antennas Wireless Propag. Lett.*, vol. 20, pp. 2554–2558, 2021.

[36] N.-W. Liu, L. Zhu, W.-W. Choi, and X. Zhang, "A low-profile aperture-coupled microstrip antenna with enhanced bandwidth under dual resonance," *IEEE Trans. Antennas Propag.*, vol. 65, no. 3, pp. 1055–1062, Mar. 2017.

[37] M. Hu and Y. Li, "Wideband back cover microstrip antenna with multiple shorting vias for mobile 5G MIMO applications," *IEEE Trans. Antennas Propag.*, vol. 71, no. 10, pp. 8290–8295, Oct. 2023.

[38] H. Zhang, L. Chang, and A. Zhang, "Extremely low-profile wideband patch antennas using electric- and magnetic-coupling for 5G mobile IoT devices application," *IEEE Antennas Wireless Propag. Lett.*, vol. 23, pp. 2698–2702, 2024.

[39] B. Cheng and Z. Du, "Dual polarization MIMO antenna for 5G mobile phone applications," *IEEE Trans. Antennas Propag.*, vol. 69, no. 7, pp. 4160–4165, Jul. 2021.

[40] X. Tian, J. Wang, C. Zheng, and Z. Du, "Shared-radiator wideband grounded patch antenna pair with bending slot for mobile terminals," *IEEE Trans. Antennas Propag.*, vol. 72, no. 4, pp. 3724–3729, Apr. 2024.

[41] Z. Cao, L. Chang, Y. Li, K. Wei, and Z. Zhang, "Dual-band decoupling between extremely closely spaced PIFAs based on LC resonator," *IEEE Trans. Antennas Propag.*, vol. 73, no. 11, pp. 8391–8399, Nov. 2025.

[42] W. Zhang, Y. Li, K. Wei, and Z. Zhang, "A dual-band MIMO antenna system for 2.4/5 GHz WLAN applications," *IEEE Trans. Antennas Propag.*, vol. 71, no. 7, pp. 5749–5758, Jul. 2023.

[43] W. Zhang, Y. Li, K. Wei, and Z. Zhang, "A high-gain dual-band multibeam antenna system for MIMO Wi-Fi application," *IEEE Trans. Antennas Propag.*, vol. 71, no. 8, pp. 6354–6364, Aug. 2023.

Jinyue Zhang received the B.S. degree from the University of Electronic Science and Technology of China, Chengdu, China, in 2024. He is currently pursuing a Ph.D. degree in electronic engineering with Tsinghua University, Beijing, China.

His current research interests include terminal antennas and wideband antennas.

Mingzhe Hu (Graduate Student Member, IEEE) received the B.S. degree in electronic engineering from Tsinghua University, Beijing, China, in 2022, where he is currently pursuing the Ph.D. degree in electronic engineering.

His current research interests include wideband antennas, low-profile antennas, and microstrip antennas.

Mr. Hu serves as a reviewer for IEEE TRANSACTIONS ON ANTENNAS AND PROPAGATION, IEEE ANTENNAS AND WIRELESS PROPAGATION LETTERS, and *Microwave and Optical Technology Letters*.

Le Chang (Senior Member, IEEE) received the B.S. degree in electronics and information engineering from Xidian University, Xi'an, China, in 2012, and the Ph.D. degree in electrical engineering from Tsinghua University, Beijing, China, in 2017.

In July 2017, he joined Huawei Technology Ltd., Beijing, as a Senior Antenna Engineer. Since 2021, he has been with Xi'an Jiaotong University, Xi'an, where he is currently an Associate Professor. He has authored or co-authored 78 journal articles. His current research interests include mobile antennas and mmW/THz antennas.

Yuehua Sun received the B.S. degree in communication engineering from Shanghai University, Shanghai, China, in 2013. He is currently pursuing the M.S. degree in engineering management with Fudan University, Shanghai.

He is also a Senior Engineer with the Hardware Technology Planning Department, Transsion Company Ltd., Shanghai. His current research interests include the development and application of terminal antennas.

Wenchao Wang received the B.S. degree in communication engineering from Xi'an Technological University, Xi'an, China, in 2007, and the M.S. degree in electronics from the University of Gävle, Gävle, Sweden, in 2013.

Since February 2022, he has been with Transsion Company Ltd., Shanghai, China, where he is currently a Senior Engineer in hardware research and development. His current research interests include the development and application of terminal antennas.

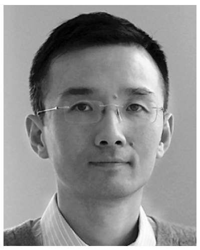

Zhijun Zhang (Fellow, IEEE) received the B.S. and M.S. degrees from the University of Electronic Science and Technology of China, Chengdu, China, in 1992 and 1995, respectively, and the Ph.D. degree from Tsinghua University, Beijing, China, in 1999.

In 1999, he was a Post-Doctoral Fellow with the Department of Electrical Engineering, University of Utah, Salt Lake City, UT, USA, where he was appointed a Research Assistant Professor in 2001. In May 2002, he was an Assistant Researcher with the University of Hawaii at Manoa, Honolulu, HI, USA. In November 2002, he joined Amphenol T&M Antennas, Vernon Hills, IL, USA, as a Senior Staff Antenna Development Engineer and was then promoted to the position of Antenna Engineer Manager. In 2004, he joined Nokia Inc., San Diego, CA, USA, as a Senior Antenna Design Engineer. In 2006, he joined Apple Inc., Cupertino, CA, USA, as a Senior Antenna Design Engineer and was then promoted to the position of Principal Antenna Engineer. Since August 2007, he has been with Tsinghua University, where he is currently a Professor with the Department of Electronic Engineering. He is the author of *Antenna Design for Mobile Devices* (Wiley, first Edition 2011, second Edition 2017).

Dr. Zhang served as an Associate Editor for IEEE TRANSACTIONS ON ANTENNAS AND PROPAGATION from 2010 to 2014 and IEEE ANTENNAS AND WIRELESS PROPAGATION LETTERS from 2009 to 2015.

Yue Li (Senior Member, IEEE) received the B.S. degree in telecommunication engineering from Zhejiang University, Zhejiang, China, in 2007, and the Ph.D. degree in electronic engineering from Tsinghua University, Beijing, China, in 2012.

In June 2012, he was a Post-Doctoral Fellow at the Department of Electronic Engineering, Tsinghua University. In December 2013, he was a Research Scholar with the Department of Electrical and Systems Engineering, University of Pennsylvania, Philadelphia, PA, USA. He was also a Visiting Scholar with the Institute for Infocomm Research (I2R), A*STAR, Singapore, in 2010, and the Hawaii Center of Advanced Communication (HCAC), University of Hawaii at Manoa, Honolulu, HI, USA, in 2012. Since January 2016, he has been with Tsinghua University, Beijing, where he was an Assistant Professor. He is currently an Associate Professor at the Department of Electronic Engineering, Tsinghua University. He has authored and co-authored over 260 journal articles and 50 international conference papers, and holds 25 granted Chinese patents. His current research interests include zero-index electromagnetics, plasmonics and metamaterials, microwave antennas, and circuits.

Dr. Li was a recipient of the Issac Koga Gold Medal from the URSI General Assembly, the IEEE APS Leopold B. Felsen Research Grant in Electromagnetics, the Second Prize of Science and Technology Award of China Institute of Communications, the Second Prize of Natural Science Award of the Ministry of Education, and Beijing Science and Technology Nova. He served as an Associate Editor for IEEE TRANSACTIONS ON ANTENNAS AND PROPAGATION from 2017 to 2024 and IEEE ANTENNAS AND WIRELESS PROPAGATION LETTERS from 2017 to 2023. He is an Associate Editor of *Microwave and Optical Technology Letters* and *Computer Applications in Engineering Education*.